CHEMISTRY OF MATERIALS

ARTICLE

pubs.acs.org/cm

Atomic Layer Deposition of $SrTiO_3$ Thin Films with Highly Enhanced Growth Rate for Ultrahigh Density Capacitors

Sang Woon Lee,[†] Jeong Hwan Han,[†] Sora Han,[†] Woongkyu Lee,[†] Jae Hyuck Jang,[†] Minha Seo,[†] Seong Keun Kim,[†] C. Dussarrat,[‡] J. Gatineau,[‡] Yo-Sep Min,[§] and Cheol Seong Hwang*[,†]

[†]WCU Hybrid Materials Program, Department of Materials Science and Engineering and Inter-university Semiconductor Research Center, Seoul National University, Seoul, 151-744, Korea

[‡]Air Liquide, 28, Wadai, Tsukuba-Shi, Ibaraki Pref., 300-4247, Japan

[§]Department of Chemical Engineering, Konkuk University, Seoul, 143-701, Korea

ABSTRACT: The ever-shrinking dimensions of dynamic random access memory (DRAM) require a high quality dielectric film for capacitors with a sufficiently high growth-per-cycle (GPC) by atomic layer deposition (ALD). $SrTiO_3$ (STO) films are considered to be the appropriate dielectric films for DRAMs with the design rule of ~20 nm, and previous studies showed that STO films grown by ALD have promising electrical performance. However, the ALD of STO films still suffers from much too slow GPC to be used in mass-production. Here, we accomplished a mass-production compatible ALD process of STO films using $Ti(O\text{-}^iPr)_2(tmhd)_2$ as a Ti-precursor for TiO_2 layers and $Sr(^iPr_3Cp)_2$ as a Sr-precursor for SrO layers. O_3 and H_2O were used as the oxygen sources for the TiO_2 and SrO layers, respectively. A highly improved GPC of 0.107 nm/unit-cycle (0.428 nm/supercycle) for stoichiometric STO films was obtained at a deposition temperature of 370 °C, which is ~7 times higher than previously reported. The origin of such high GPC values in this STO films could be explained by the partial decomposition of the precursors used and the strong tendency of water adsorption onto the SrO layer in comparison to the TiO_2 layer. The STO film grown in this study also showed an excellent step coverage (~95%) when deposited inside a deep capacitor hole with an aspect ratio of 10. Owing to the high bulk dielectric constant (~ 146) of the STO film, an equivalent oxide thickness of 0.57 nm was achieved with a STO film of 10 nm. In addition, the leakage current density was sufficiently low (3×10^{-8} Acm^{-2} at +0.8 V). This process is extremely promising for fabrication of the next generation DRAMs.

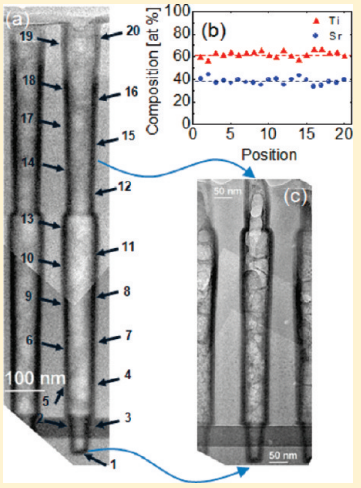

KEYWORDS: Capacitor, DRAM, $SrTiO_3$, Ru, ALD, deposition rate

I. INTRODUCTION

The further scaling of dynamic random-access memory (DRAM) to a design rule <30 nm is being hindered by the stringent requirements of cell capacitance, with an extremely small capacitor size. The technology roadmap requires an extremely low equivalent oxide thickness (EOT) value <0.5 nm while maintaining a low leakage current. For these requirements, $SrTiO_3$ (STO) thin films must be the ultimate material of choice to overcome the limitations of the current ZrO_2-based dielectrics[1,2] as well as the newly highlighted Al-doped TiO_2,[3] because it has a dielectric constant >100 even at a low film thickness (~ 10 nm). Because physical[4−7] and chemical vapor deposition (CVD) methods[8−13] cannot meet the stringent conformality, atomic layer deposition (ALD) has been highlighted.[14−17] ALD, which is characterized by its unique self-limiting deposition mechanism, can be used to grow dielectric films as well as metal electrodes on account of its excellent conformal step coverage over the severe three-dimensional (3D) structure with a high aspect ratio in DRAM capacitors.

Development of Sr-precursors for ALD has been hindered by the complicated ALD chemistry of these groups, which comes from the low volatility, poor thermal stability, and weak reactivity to surface functional groups of these materials.[18] In practice, the selection of Sr-precursor has been restricted to β-diketonate and cyclopentadienyl compounds.[16,18] Although the most viable Sr-precursor has been $Sr(tmhd)_2$ (tmhd = 2,2,6,6-tetramethyl-3,5-heptanedionate), they unfortunately show a very limited ALD reactivity with H_2O.[18] Therefore, an oxygen source with higher reactivity such as O_3 has been used to induce a more active ALD reaction with the $Sr(tmhd)_2$ precursor.[19] However, $SrCO_3$ films were grown instead of SrO, which could not be alleviated even by combining TiO_2 layer growth.[19] Kim et al. used O_2-plasma for the same Sr-precursor, and achieved almost carbonate-free STO films in ALD mode with promising electrical properties after the appropriate postdeposition annealing (PDA) step to crystallize them.[20] However, a plasma-based ALD process has a potential concern regarding the step coverage over a severe

Received: January 26, 2011
Revised: March 8, 2011
Published: March 30, 2011

3D geometry. The authors reported that the SrO layer can be grown on a TiO_2 surface even with the $Sr(tmhd)_2 + H_2O$ chemistry as a result of the catalytic effect of the TiO_2 surface, and stoichiometric STO films were grown by appropriate control of the SrO/TiO_2 cycle ratio.[21]

Recently, Menou et al. and Pawlak et al. reported another promising ALD route to form STO film using $Sr(^iBu_3Cp)_2$ ($^iBu_3Cp$ = trisisobuthylcyclopentadienyl) and $Ti(OMe)_4$ (OMe = methoxide), as the Sr- and Ti-precursors, respectively, and H_2O as the oxygen source at a typical T_g of 250 °C on TiN electrode.[16] In those works, the as-grown films were amorphous due to the low growth temperature, and the PDA step was necessary. The cation-stoichiometric films showed micro- and nanoscale cracks after the PDA so that the electrical properties were not promising. They found that the inclusion of extra SrO layer in the film by depositing Sr-rich film (Sr/(Sr+Ti) ~62 at. %) efficiently suppresses the crack formation during the PDA and leakage current density was largely decreased. However, the dielectric constant of this Sr-rich film was only ~60−70 implying the potential limit of this process. Therefore, it is believed that the high-temperature ALD process that may give the in situ crystallization is still necessary. By the way, the adoption of TiN electrode, instead of noble metal Ru electrode, is a crucial merit of the works in ref 16. However, the impact of higher ALD temperature on the possible oxidation of TiN electrode was not reported.

Although there are several reports on the growth of the STO films by ALD,[14−22] there are few reports on the concurrent achievement of the useful electrical properties, conformal step coverage as well as the high ALD growth rate to satisfy the stringent requirements of DRAM fabrication. This is generally attributed to the fact that ALD proceeds at low growth temperatures, which is not compatible with achieving in situ crystallization and a high density. As-deposited amorphous films with a low density generally result in undesirable properties after crystallization annealing due to film shrinkage and accompanying microcracking.[21,22] The authors recently reported that the in situ crystallization of STO at the as-deposited state could be achieved by increasing the deposition temperature as high as possible within the ALD regime and adopting a crystalline seed layer.[21] The resulting electrical properties were promising. From a Pt/20-nm-thick STO/Ru(bottom) capacitor, an EOT of 0.72 nm and a low leakage current density ($\sim 10^{-7}$ Acm^{-2} at 0.8 V) were achieved. In that study, $Ti(O^iPr)_2(tmhd)_2$ (O^iPr = isopropoxide), which is thermally more stable than $Ti(O^iPr)_4$, was adopted as a Ti-precursor while the same $Sr(tmhd)_2$ was used as a Sr-precursor. These precursors allowed the growth of TiO_2 and STO films on $Ru/SiO_2/Si$ substrates at a growth temperature (T_g) as high as 390 °C in ALD mode.[21] However, the growth per cycle (GPC) of 0.015 nm/cycle was too low to be used in mass production. This was attributed mainly to the very low chemical reactivity between the $Sr(tmhd)_2$ and H_2O. Therefore, an alternative Sr-precursor with better chemical reactivity and thermal stability is needed for the development of a mass-production compatible STO ALD process.

With this regard, the cyclopentadienyl (Cp) ligand based Sr-precursor, such as $Sr(^iPr_3Cp)_2$ ($^iPr_3Cp$ = 1,2,4-trisisopropylcyclopentadienyl), is of high interest. It generally has a higher vapor pressure than $Sr(tmhd)_2$ which facilitates the fluent delivery of the precursor to the ALD chamber. The chemical bond energy between the Sr ion and Cp ligand is much weaker than that between the Sr ion and tmhd ligand.[23] Holme et al. reported that the energy required to break the bond between the first Cp and Sr is ~2.58 eV and that between the first tmhd and Sr is ~4.94 eV. This low bonding energy of Cp to Sr may allow the more fluent removal of the ligands during the chemical adsorption of the Sr-precursor molecules which may result in a higher GPC. However, the thermal decomposition of the Cp ligand should also be considered. If the decomposed Sr-species are not sufficiently volatile after a partial decomposition, they may also enhance the GPC at higher growth temperatures due to the CVD-like growth of films. This may result in an undesirable characteristic of the Cp-based precursors for the in situ crystallization process of the ALD STO films.

According to the report by Holme et al., in alkyl-substituted Cp, the weakest bond is the bond between the nearest neighboring alkyl carbon and the next nearest neighboring alkyl carbon to the Cp ring, of which the bond energy is ~1.48 eV in the case of *n*-propylcyclopentadienyl. On the other hand, the bond energy (~4.89 eV) between the nearest neighboring alkyl carbon and the Cp ring is much higher than the binding energy of Cp and Sr. Therefore, even if the $^iPr_3Cp$ ligand is partially decomposed during the ALD process, the partially decomposed Sr-species may still be volatile because of the methyl groups remaining in the Cp ring. Thus, the partial decomposition of the $^iPr_3Cp$ ligand may not result in the CVD-like growth of the film.

The chemical reaction route for the ligand exchange reaction of such a complex organometallic compound is generally complicated and may heavily depend on the oxygen source used. The typical oxygen sources in ALD of oxides, H_2O and O_3, have quite distinctive chemical influence on the ALD of oxide thin films. The GPC of SrO (or $SrCO_3$) layers from $Sr(tmhd)_2$ is much higher when using O_3 as the oxidant than when using H_2O as the oxygen source.[18,19] Similarly, the GPC of ALD TiO_2 films using $Ti(O^iPr)_2(tmhd)_2$ can also be increased by using O_3 instead of H_2O.[24] However, it was found, in this study, that the GPC of the SrO layer from the $Sr(^iPr_3Cp)_2$ precursor is much higher when using H_2O than when using O_3. In addition, it was also interesting to note that the grown layers have almost no carbon contamination by undesired chemical reactions such as strontium carbonate formation, which is commonly observed when the chemistry of $Sr(tmhd)_2$ and O_3 is used for the SrO layer. Furthermore, the ALD temperature window for SrO and STO deposition was also quite dependent on the type of oxygen source used. Therefore, $Sr(^iPr_3Cp)_2$ is a highly intriguing precursor in terms of ALD chemistry as well as the material properties of the grown films.

In this study, $Sr(^iPr_3Cp)_2$ was used as an alternative Sr-precursor to achieve STO films with a high GPC. The weakly bound $^iPr_3Cp$ ligand in this Sr-precursor was preferable for a facile ALD reaction to occur so that a much higher GPC of STO ($\sim$ 7 times higher than the previous GPC from $Sr(tmhd)_2$) was achieved. The STO films show an EOT of 0.57 nm with a stably low leakage current (3×10^{-8} Acm^{-2} at 0.8 V) on Ru electrode as well as an excellent step coverage of 95% inside a deep capacitor hole with an aspect ratio of 10. These highlight the extreme value of the STO films by this ALD process for the next generation DRAM capacitor fabrication.

II. EXPERIMENTAL SECTION

A 4-in.-diameter single wafer traveling-wave type ALD reactor (CN-1 Co, Plus-100) was used to grow TiO_2 and STO films. The bubblers for

the Ti- and Sr-precursors were heated to 130 and 110 °C, respectively. $Sr(^iPr_3Cp)_2$ was developed and manufactured by the Air Liquide company. The precursors were delivered to the ALD chamber with the assistance of Ar carrier gas at a flow rate of 200 sccm. The working pressure was 0.7 Torr. H_2O or O_3 was used as the oxygen source. H_2O was cooled down to 3 °C to control its high vapor pressure. The O_3 concentration was 320 gm^{-3}. The typical ALD process consisted of a precursor pulse (3 s)−Ar purge (5 s)−oxygen source pulse (2 s)−Ar purge (5 s). Sputter-deposited Ru(30 nm)/Ta_2O_5(8 nm)/thermally oxidized SiO_2(100 nm)/Si wafers were used as substrates. The physical thickness of the STO films was measured using an ellipsometer, and the layer density and cation composition were confirmed by X-ray fluorescent spectroscopy (XRF, Themoscientific, ARL Quant'X). The impurity concentration, including carbon, in the films was examined by Auger electron spectroscopy (AES, Perkin-Elmer 660). The film surface morphology was examined by field-emission scanning electron microscopy (FESEM, Hitachi S-4800). The chemical binding states of the films were determined by X-ray photoelectron spectroscopy (XPS, ThermoVG, SIGMAPROBE). The crystal structure of the film was investigated by glancing angle mode X-ray diffraction using a Cu Kα X-ray source (GAXRD, PANalytical, X'pert Pro). The incidence angle, scan step size, and time per step during the GAXRD measurement were 2°, 0.01°, and 0.5 s, respectively. The density of the films was estimated by X-ray reflectivity (XRR) measurements using a Cu Kα X-ray source. High-resolution TEM (HRTEM, JEOL 3000F) equipped with energy-dispersive spectroscopy (EDS) was used to analyze the thickness and compositional step coverage of the STO film on the contact hole structure. Annealing was performed in a rapid-thermal-annealing system at 650 °C for 1 min in a pure N_2 atmosphere (purity >99.99%). The planar structured metal−insulator−metal capacitors were fabricated by depositing an 80-nm-thick top Pt electrode through a shadow mask (0.3 mm hole diameter). Cure-annealing was performed after depositing the top Pt electrode at 400 °C in air for 30 min. The electrical properties, including the capacitance and leakage current, were measured using a HP 4194A impedance analyzer at 10 kHz and a HP 4140B picoammeter, respectively.

III. RESULTS AND DISCUSSION

Growth of STO Films Depending on the ALD Sequences. Figure 1a−d shows the process sequences for the deposition of TiO_2, SrO, and STO thin films. The TiO_2 growth sequences are abbreviated as TH and TO for the deposition with H_2O and O_3 as the oxygen sources, respectively. The abbreviations SH and SO are used for the deposition of SrO films (Figure 1c), and TOSH is used for the deposition of STO in the same way.

The authors reported recently that growth of TiO_2 film using $Ti(O^iPr)_2(tmhd)_2$ was possible at a T_g as high as 390 °C in ALD mode irrespective of the oxygen source type, and the GPC of TiO_2 film with a TO sequence was higher than that of the TH sequence at all T_g.[24] The origin of such a different saturated GPC for the two oxygen sources was assigned to the limited reactivity between the chemisorbed Ti-species (possibly $Ti(tmhd)_2$) and H_2O due to the strong bond energy between the tmhd ligand and Ti ion which eventually hinder the effective adsorption of the Ti precursor during the Ti-precursor exposure step.[25]

Figure 2a shows the growth characteristics of SrO films with the sequences SH and SO, respectively, with deposition cycles of 33 on a Ru substrate. The inset figure shows the same plot in Arrhenius form. Here, the layer density of Sr measured by XRF was used to compare the deposition rate because the ellipsometric thickness of SrO film is unreliable due to the severe formation of carbonate or hydroxide on SrO when the film was taken out of the ALD reactor.[18]

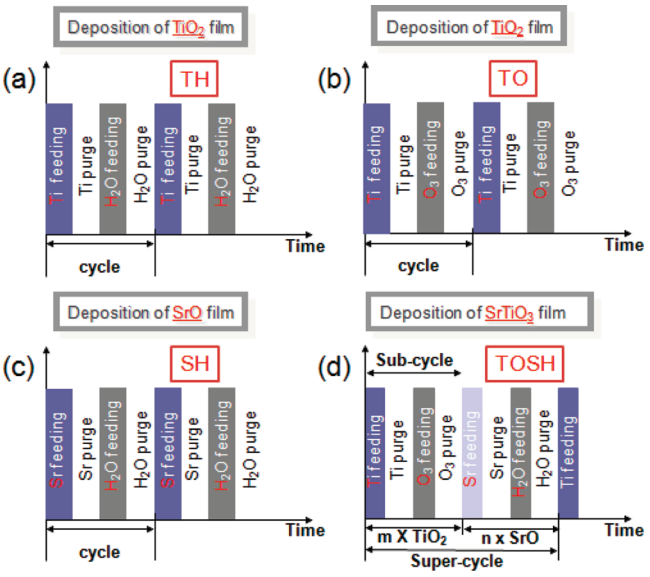

Figure 1. Process sequence for the deposition of TiO_2, SrO, and STO films. The abbreviated growth sequence was used as (a) TH and (b) TO for the deposition of a TiO_2 film when H_2O and O_3 were used as the oxidants, respectively. The abbreviated growth sequence was also used as (c) SH for the deposition of SrO film, and (d) TOSH for the deposition of a STO film in the same way, respectively.

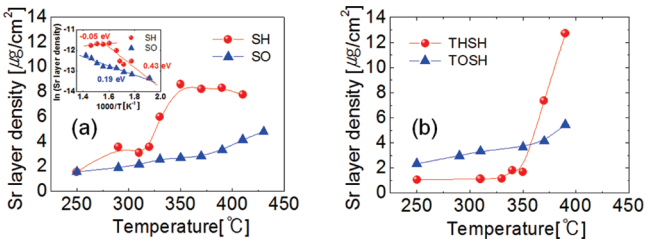

Figure 2. (a) Growth characteristics of SrO films with the sequences of SH and SO with deposition cycles of 33 on a Ru substrate. (Inset) Same plot with the Arrhenius form and (b) the changes in the layer density of STO films as a function of T_g with the sequences THSH and TOSH, respectively.

$Sr(^iPr_3Cp)_2$ showed higher reactivity toward H_2O than O_3 over the whole T_g range as shown in Figure 2a, which is an opposite tendency compared to the GPC behavior of SrO (or $SrCO_3$) obtained from $Sr(tmhd)_2$.[18,19] This can be explained by the low bond energies between $^iPr_3Cp$ and Sr. Holme et al. reported that the energies required to break the bonds between $^iPr_3Cp$ and Sr are 2.58 eV for the first $^iPr_3Cp$ and 1.40 eV for the second $^iPr_3Cp$. However, in $Sr(tmhd)_2$, the bond energies for the first and second tmhd ligands are 4.94 and 3.75 eV, respectively. Therefore, it is expected that the chemisorbed Sr-$^iPr_3Cp$ (ads) may have much smaller bond energy than that of the chemisorbed Sr-tmhd (ads), and that the Sr-$^iPr_3Cp$ (ads) is much more labile to the ligand exchange reaction by H_2O than Sr-tmhd (ads) is. On the other hand, for the O_3 process (i.e., SO), it was recently reported that O_3 exposure on the metal−ligand (ads) leads to the formation of mainly formate and carbonate species on the surface, which are expected to be less reactive toward $Sr(^iPr_3Cp)_2$.[26−28] In addition, it should be noted that Sr atoms on the surface are still unsaturated due to its high coordination

dx.doi.org/10.1021/cm2002572 |Chem. Mater. 2011, 23, 2227–2236

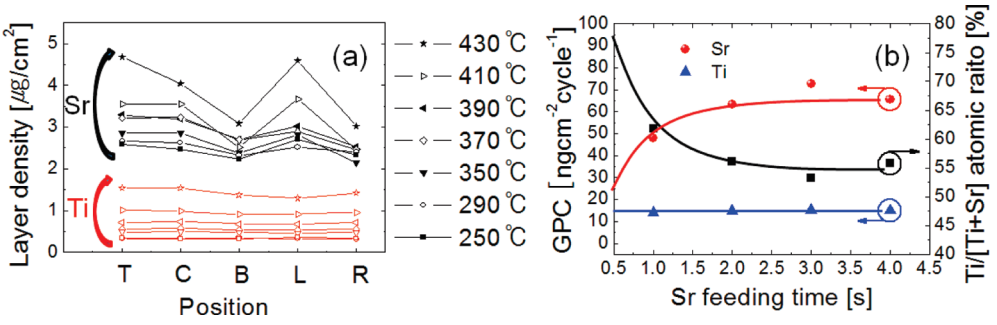

Figure 3. (a) Layer densities of Sr and Ti in STO films at various locations (T: top, C: center, B: bottom, L: left, R: right position) within a 4-in.-diameter wafer as a function of T_g and (b) changes in the GPC and Ti concentration in the growth of STO films (cycle ratio of 3:1) grown at 370 °C on Si as a function of the Sr-precursor feeding time (t_{Sr}) for the given Ti-precursor input time (t_{Ti}) of 3 s.

number. Therefore H_2O exposure may form H_2O adducts on the surface Sr atoms which may enhance the adsorption of $Sr(^iPr_3Cp)_2$ during the subsequent exposure of Sr-precursors. Indeed, the preferred adsorption of H_2O on the SrO layer in the STO crystal surface was experimentally observed by friction force microscopy and also theoretically calculated recently.[29,30]

From the inset figure of Figure 2a, it can be recognized that there are two kinds of activation regions above (activation energy $E_a \approx 0$ eV) and below ($E_a \approx 0.43$ eV) 350 °C in the sequence SH. Although the data are scattered below 350 °C, the general tendency shows an increasing layer density of Sr in this temperature region. This may possibly come from the partial decomposition of $Sr(^iPr_3Cp)_2$ to a smaller alkyl-substituted Cp complex (e.g., trimethylcyclopentadienyl). As mentioned in the Introduction, the weakest bond of the $^iPr_3Cp$ ligand is the bond between the nearest neighboring alkyl carbon and the next nearest neighboring alkyl carbon to the Cp ring. In addition, the partial decomposition of the $^iPr_3Cp$ ligand might be catalyzed in the presence of the H_2O adducts because the abrupt increase of the Sr layer density was not observed in the SO process. It should be noted that the H_2O adducts can be decomposed to H_2 and O and removed by O_3 exposure.

At around 350 °C, most isopropyl groups of $Sr(^iPr_3Cp)_2$ may be decomposed to methyl groups. Because the resulting methyl-substituted Cp complexes are still volatile enough to induce the self-limiting growth of SrO, a high temperature region with a small activation energy can be observed, which can be explained by the reduced amount of steric hindrance the methyl-substituted Cp complex experiences when reacting with the surface hydroxyl groups. This is highly promising because the in situ crystallization of STO requires a higher T_g, as previously reported.[21]

Figure 2b shows the changes in layer density of STO films as a function of T_g with the sequences THSH and TOSH, respectively. As in the case of SrO film growth with the sequence SH, the layer density of Sr was increased drastically at ~350 °C in the case of the sequence THSH. However, in the case of the sequence TOSH, the layer density of Sr increased slightly with increasing T_g up to ~400 °C. This is similar to the SrO film growth behavior with the sequence SO shown in Figure 2a. In the sequence TOSH, $Sr(^iPr_3Cp)_2$ molecules are adsorbed on the O_3-treated surface (i.e., formate- and/or carbonate-containing surface) for the previous TiO_2 layer growth, even though H_2O was used as the oxygen source for $Sr(^iPr_3Cp)_2$. Therefore, it is reasonable to have a SrO layer with a similar growth behavior in the growth of STO films using the sequence TOSH. Accordingly,

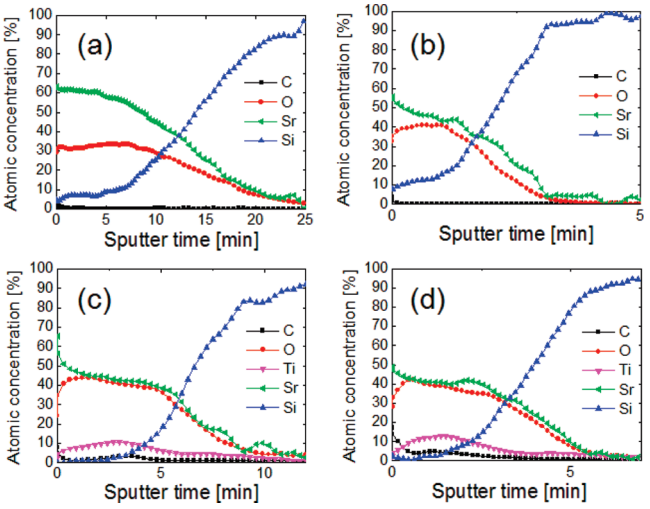

Figure 4. AES depth profiles of the SrO and STO films grown with the sequences (a) SH, (b) SO, (c) TOSH, and (d) TOSO.

the sequence TOSH was chosen for the growth of STO films. H_2O was chosen as the oxygen source for $Sr(^iPr_3Cp)_2$ to minimize the formation of Sr−carbonate phase.[19] The sequence TOSO resulted in a higher level of carbon residue in the film (see Figure 4d), thus, it is not used in this study.

Interestingly, the increase of Sr layer density below 350 °C in the THSH process is much smaller than that in the SH process. This also supports the idea that the partial decomposition of the $^iPr_3Cp$ ligand is catalyzed in the presence of H_2O adducts. It should be noted that the H_2O molecules pulsed on the Ti−O surface (in the TH step) was consumed to form the Ti−O−H group so that adduct H_2O cannot be provided to the subsequently supplied Sr-precursors.

Figure 3a shows the layer densities of Sr and Ti in the STO film at various locations within the 4-in.-diameter wafer. The Ti in STO showed good uniformity up to 390 °C, but deteriorated slightly above that temperature. The degradation of the within-wafer uniformity suggests the involvement of the CVD component from this temperature due to the cross-flow type geometry of the ALD reactor. The within-wafer uniformity of Sr in STO also suddenly became worse over 390 °C, suggesting that this temperature is also the upper bound of the ALD temperature window. The GPC of STO varies in the range of 0.07−0.13 nm/cycle depending on the ALD temperature window (not shown here).

dx.doi.org/10.1021/cm2002572 |Chem. Mater. 2011, 23, 2227–2236

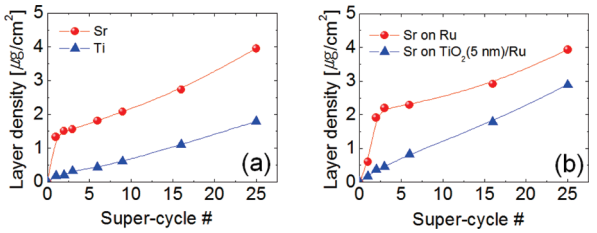

Figure 5. (a) Changes in the layer density of Sr and Ti on Ru substrate as a function of the number of supercycles. Here, 1 supercycle is composed of 5 TiO_2 cycles and 1 SrO cycle. (b) Changes in the layer density of STO films grown on Ru and TiO_2-covered Ru substrates under the same deposition conditions. The exaggerated incorporation of Sr on a Ru substrate could be blocked by depositing a thin (5-nm-thick) TiO_2 layer by ALD on a Ru substrate.

Figure 3b shows the changes in the GPC and Ti concentration in the growth of STO films (cycle ratio of 3:1) grown at 370 °C on Si as a function of the Sr-precursor feeding time (t_{Sr}) for the given Ti-precursor input time (t_{Ti}) of 3 s, which is a well-setup condition for TiO_2 film deposition.[21,24] First, a constant Ti concentration could be achieved irrespective of t_{Sr} when $t_{Sr} > 2$ s, where the amount of Sr was saturated, which is the crucial merit of the ALD process compared to CVD. Interestingly, the amount of Ti incorporated in the STO film was not changed by increasing t_{Sr} for a given t_{Ti} of 3 s, which shows a different growth behavior compared to the $Sr(tmhd)_2$ case.[21] In a previous report, the amount of Ti decreased with increasing t_{Sr} for a given t_{Ti}, which was attributed to the residual ligand from the incomplete reaction of $Sr(tmhd)_2$ with H_2O. The lack of an effect of t_{Sr} on the amount of Ti suggests that the growing SrO layer from the reaction of $Sr(^iPr_3Cp)_2$ and H_2O did not hinder the subsequent growth of TiO_2. This indicates that the reactivity of $Sr(^iPr_3Cp)_2$ is high enough to lead a complete and clean ALD-type reaction.

Figures 4a–d shows the AES depth profiles of the SrO and STO films grown at 370 °C with the sequences SH, SO, TOSH, and TOSO, respectively. The residual carbon concentration was <1 at. % in SrO irrespective of the oxygen source, suggesting that $SrCO_3$ growth was suppressed efficiently with this Sr-precursor. The carbon content was increased slightly to 1–2 at. % in STO with the sequence TOSH, which might be due to carbon incorporation from the TiO_2 growth cycle (Figure 4c). The residual carbon content was increased slightly to 3–4 at. % in the TOSO sequence, suggesting that the use of O_3 for both precursors increases the risk of carbonate contamination (Figure 4d).

Exaggerated Incorporation of Sr on Ru Substrate during the Initial Growth and Its Control. STO thin film growth was examined in detail with the sequence TOSH on Ru substrate at 370 °C. Figure 5a shows the changes in the layer density of Sr and Ti on Ru substrate as a function of the number of supercycles. Here, 1 supercycle was composed of 5 TiO_2 cycles and 1 SrO cycle. The Ti incorporation in the film was linear over the entire supercycle range with negligible incubation cycles. On the other hand, Sr incorporation in the film was exceptionally high on the Ru substrates during the initial 1–2 supercycles, which then approached the steady state growth mode afterward. This suggests that the Sr-precursors interact strongly with the Ru substrate at the initial growth step. Another set of STO films was grown again on the Ru and TiO_2-covered Ru substrate under the same deposition conditions (Figure 5b). The accelerated incorporation of Sr also occurred during the initial 3 supercycles but

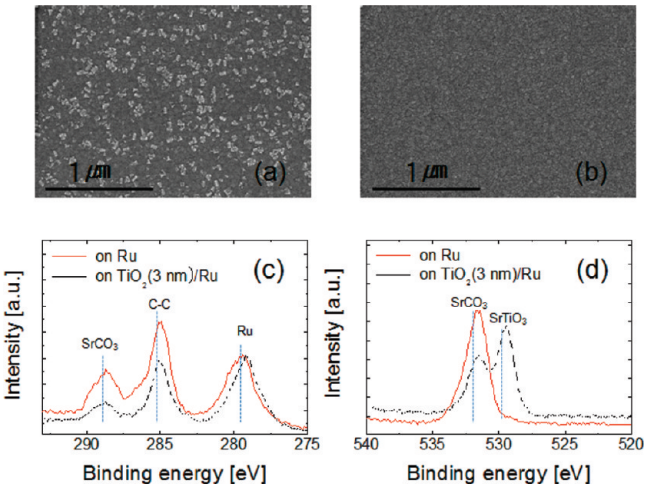

Figure 6. Surface morphology of 17-nm-thick STO films grown on the (a) Ru and (b) TiO_2-coated Ru substrate. The film on the Ru substrate shows many irregular shaped small particles, which appear to be $SrCO_3$. XP spectra of (c) C 1s and (d) O 1s of the films grown on Ru and TiO_2-coated Ru substrates by 2 and 6 supercycles, respectively.

the process repeatability during such an initial growth stage was somewhat uncontrollable, as can be understood from the different layer density from that in Figure 5a below a supercycle number < ~10. However, this exaggerated incorporation of Sr on the Ru substrate could be blocked by depositing a thin (5-nm-thick) TiO_2 layer by ALD on the Ru substrate, as shown in Figure 5b.

The accelerated incorporation of Sr at the initial growth step on Ru was examined in more detail. Figure 6a and b show the surface morphology of 17-nm-thick STO films grown on the Ru and TiO_2-coated Ru substrate, respectively. The film on the Ru substrate showed many irregular shaped small particles, which appear to be $SrCO_3$, as shown in Figure 6c and d. No such particles were observed on the TiO_2-coated Ru substrate. Figure 6c shows the XP spectra of C 1s on the films grown on Ru and TiO_2-coated Ru substrates using 2 and 6 supercycles, respectively (1 supercycle = 5 TiO_2 cycle +1 SrO cycle). The XPS peak positions were calibrated using the adventitious C 1s peak position (C–C bonding, 285.0 eV).[31] The binding energy of 288.7 eV corresponds to $SrCO_3$. The film grown on the Ru substrate had stronger Sr–carbonate component than that on the TiO_2-coated Ru substrate. A small $SrCO_3$ peak was observed in the case of the TiO_2-coated Ru substrate because $SrCO_3$ was also formed on the film surface as the sample was exposed to air for a few hours prior to the XPS measurements. When the STO film was directly grown on the Ru electrode, thin interfacial $SrRuO_3$ appears to form, which can be understood from the shift of the Ru 3d peak into the higher binding energy direction. The presence of a Sr–carbonate component in the film was confirmed by a comparison of the O 1s spectra of two samples (Figure 6d). The binding energy of 529.2 and 531.5 eV corresponds to $SrTiO_3$ and $SrCO_3$, respectively. There was almost no O 1s signal corresponding to STO when the film was grown on Ru suggesting that the incorporated Sr atoms form only $SrCO_3$. On the other hand, the majority of the O 1s peak originated from the STO phase when the film was grown on TiO_2-coated Ru, whereas the minor $SrCO_3$ peak might be assigned to the surface Sr–carbonate due to air exposure.

dx.doi.org/10.1021/cm2002572 |Chem. Mater. 2011, 23, 2227–2236

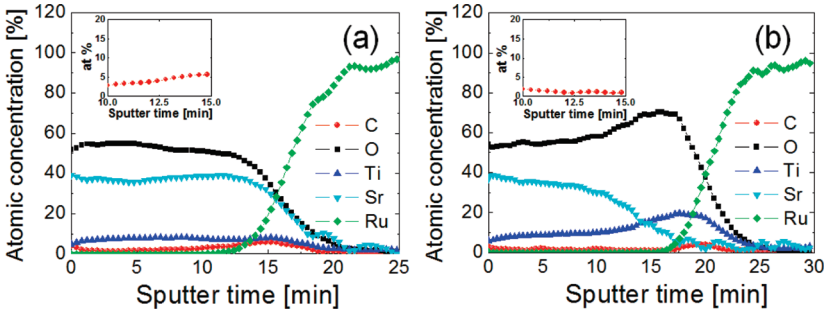

Figure 7. AES depth profile results of the 17-nm-thick STO films grown on (a) Ru and (b) TiO_2-coated Ru. Inset figures show the enlarged portion of the C profiles near STO/Ru and STO/TiO_2/Ru interfaces.

The AES depth profile results of the 17-nm-thick STO films grown on Ru and TiO_2-coated Ru, shown in Figures 7a and b, respectively, further confirmed the XPS results. The C concentration in the Ru layer appears high in both cases due to overlap of the C and Ru Auger peaks. Therefore, the data in the region over the Ru layer were examined more closely. There was a negligible C concentration in the bulk STO layer in both cases. However, there was a higher C concentration on the Ru layer for Figure 7a (compare the insets of Figure 7a and b). This suggests that $SrCO_3$ was formed on the Ru surface when the STO film was grown directly on Ru, which could be suppressed effectively when grown on the TiO_2-coated Ru surface.

Origin of the Peculiar Growth Behavior of STO Film on Ru Substrate. To understand the peculiar behavior of STO film growth on a Ru substrate, the following experiments were performed assuming that the oxidized Ru surface plays an important role on the growth of TiO_2 and SrO layers.

The STO films were grown on seven different substrates, IrO_2, RuO_2, Ru, Pt, TiO_2, SiO_2, and Si, with the Ti/Sr cycle ratio of 5:1 under identical ALD conditions. Here, Ru and Pt were dc sputtered, IrO_2 was reactively sputtered under an Ar/O_2 gas atmosphere, and RuO_2 and TiO_2 were grown by an ALD. SiO_2 was grown thermally in a furnace. STO deposition was started with five consecutive pulses of TiO_2 cycles followed by one SrO cycle. Figure 8a shows the change in the Ti layer density as a function of the number of supercycles on various substrates. Ti incorporation on the IrO_2 surface was quite excessive during the first supercycle, and the growth rate decreased rapidly and reached a saturation value from the second supercycle, where the saturated growth rate was similar to those on the other substrates. A similar phenomenon was also observed on the RuO_2 substrate but with less excessive initial growth. Other substrates showed a similar saturated growth rate with negligible initial growth exaggeration. The details for such an abnormal ALD behavior of Ti-incorporation in the ALD of TiO_2 film by the same process recipe were recently reported by the same authors, where the oxygen in the Ru- and Ir-containing substrates plays the key role.[24] Similar reasoning can be used for this case as shown below.

The incorporation of Sr into the film showed a behavior somewhat similar to that of Ti on the various substrates, as shown in Figure 8b. However, there are some discrepancies from that of Ti. The RuO_2 substrate showed the highest initial growth rate. IrO_2 and Ru showed a similar initial exaggerated growth rate but to a lesser extent. The other substrates did not show an initial increase in growth rate. The change in chemical status of the IrO_2 and Pt substrates, which represent high initial growth and no

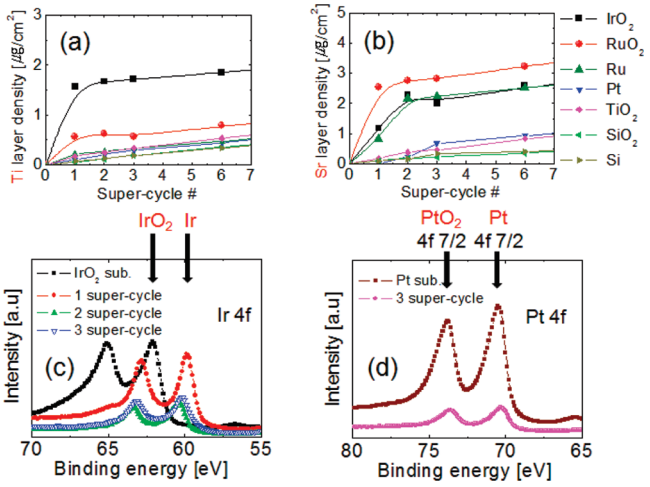

Figure 8. Change in the (a) Ti and (b) Sr layer density as a function of the supercycle number on various substrates (IrO_2, RuO_2, Ru, Pt, TiO_2, SiO_2, and Si substrates), respectively. (c) XP spectra of Ir 4f before and after the deposition of STO on IrO_2 substrate with 1, 2, 3 supercycles. The binding energy of the Ir 4f 7/2 of IrO_2 (62.1 eV) was shifted to much lower binding energies of metallic Ir (∼ 60.2 eV) after the deposition of STO, which indicates the reduction of the IrO_2 substrate. (d) No change in the binding energy of the Pt substrate before and after the deposition of STO.

initial growth enhancement substrates, respectively, after 1, 2, and 3 supercycles of STO ALD was examined by XPS. Figure 8c shows that the IrO_2 surface was almost completely reduced to Ir (ref 32) after only one supercycle. On the other hand, the Pt surface did not show any change in the chemical status even after 3 supercycles as expected from the chemical inertness of Pt (Figures 8d).

The almost complete reduction of IrO_2 can be understood from its smaller Gibb's free energy of formation than the other compounds, as shown in Table 1.[33] When the Ti or Sr precursor molecules were pulsed onto the IrO_2 surface, the Ti or Sr metal ions extracted oxygen atoms from IrO_2 due to the stronger oxidation potential of TiO_2 or SrO than IrO_2. This coincides with the circumstance that a large amount of active oxygen atoms is supplied to the growing surface during the precursor pulse step, even though no O_3 or H_2O gas is supplied. This can induce a CVD type reaction during the initial growth step as reported recently for the TiO_2 ALD,[24] which can incorporate a much larger amount of oxide material compared to the saturated GPC. The saturated GPC was achieved at a higher supercycle number, where the substrate was covered completely with the growing

Table 1. Standard Formation Energy of the Various Materials at 600 K

material	ΔG_f (600 K, kJ/mol)
IrO_2	−134.765
RuO_2	−201.190
PtO_2	164.065
SiO_2	−801.367
TiO_2	−833.972
SrO	−530.946
$SrTiO_3$	−1502.305
$SrCO_3$	−1057.595

STO layer. The highest and second-highest initial growth rate of the TiO_2 layer on the IrO_2 and RuO_2 substrates during the first supercycle can be understood from the lowest and second-lowest thermal stability of IrO_2 and RuO_2 over TiO_2 (Table 1). A similar increase in the initial growth rate of the TiO_2 film on a Ru electrode was reported by Won et al. when a TiO_2 film was grown by ALD at a T_g of 250 °C using $Ti(OC_3H_7)_4$ and N_2O and the precursor and plasma oxygen source, respectively.[34] They attributed the enhanced initial growth to the oxygen supply from the in situ oxidized Ru substrate during TiO_2 ALD. However, no initial growth enhancement of Ti was observed on Ru in the present study. In the previous study of TiO_2 ALD using the same precursor and O_3, the initial enhancement effect was observed on Ru electrode but with a much less extent compared with the case of RuO_2 substrate (Figure 7 of ref 24). This suggests that the oxygen supply effect from the in situ oxidized Ru is quite weaker than that from the RuO_2 layer. In this experiment, the consumption of oxygen from the in situ oxidized Ru is shared with Sr atoms, and H_2O was used for SrO layer growth. Therefore, the initial enhancement effect of Ti-incorporation could be almost negligible for Ru substrate.

The initial growth enhancement of the SrO layer on IrO_2, RuO_2, and Ru can be understood by the similar oxygen supply model from the substrate layers. However, the different degree of enhancement depending on the types of substrates from those of the TiO_2 layer requires additional consideration. The Sr-precursor has a higher tendency to crack thermally at this temperature compared to the Ti-precursor when oxygen source is supplied (Figure 2).[24] In addition, SrO is more oxygen scavenging than TiO_2 (Table 1). Therefore, SrO layer growth is more prone to a CVD type reaction on reduction-facile substrates (IrO_2, RuO_2, and even Ru) compared to that on a TiO_2 layer. The smaller initial growth enhancement of the SrO layer on IrO_2 compared to RuO_2 can be understood from the following. During the initial five consecutive subcycles of TiO_2 growth, most of the oxygen atoms on the IrO_2 surface were already taken by the TiO_2 layer, and little oxygen was left to enhance SrO growth during the subsequent first SrO growth step. Therefore, the only way that the extra oxygen can be supplied to the growing surface is the in situ oxidation of Ir during the O_3 step after the Ti-precursor pulses and reduction of it during the Sr-precursor pulse step. A similar process appears to occur on Ru as can be understood from the similar growth enhancement of SrO. The different thickness of the TiO_2 layer grown during the initial five TiO_2 steps on the different substrates (IrO_2 and RuO_2 in Figure 8a) barely affects the oxidation and reduction of the underlying Ir or Ru layers and the consequent enhancement of SrO layer growth owing to their extreme thinness and high

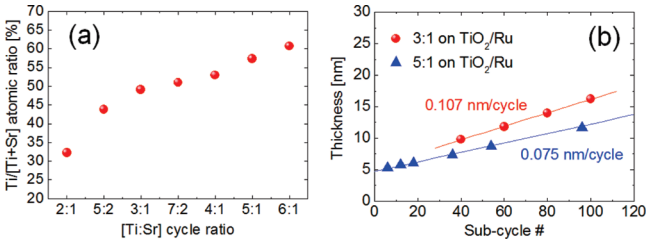

Figure 9. (a) Wide compositional variation on the TiO_2-coated Ru substrate with high repeatability and accuracy by changing the Ti and Sr cycle ratio. (b) Changes in the STO film thickness as a function of the subcycle number on a 5-nm-thick TiO_2 coated Ru substrate when the Ti:Sr cycle ratio was 3:1 and 5:1, respectively. The steady state GPC of STO was 0.075 and 0.107 nm/cycle at a cycle ratio of 5:1 and 3:1, respectively.

oxygen mobility.[34] The growth enhancement of the SrO layer on the RuO_2 substrate was the highest, suggesting that oxygen atoms remain on the RuO_2 surface after the TiO_2 steps and are supplied to the Sr-precursor molecules during the Sr-precursor pulse step. This is due to the less scavenging of oxygen atoms during the previous TiO_2 ALD steps. It must be noted that RuO_2 has slightly higher formation energy than that of IrO_2. Therefore, a small portion of oxygen can be left in the Ru(O) layer even after the TiO_2 steps are completed, and the subsequent SrO step can be enhanced by the stronger oxidation potential of SrO. The other oxygen-nonsupplying substrates did not show any initial growth enhancement effect.

The formation of $SrCO_3$ on the Ru surface can be understood from these results. The excessive supply of oxygen atoms to the adsorbing Sr-precursor molecules by the in situ oxidation and subsequent reduction of Ru can form CVD type SrO layers and CO_2 gas by decomposition of the cracked Cp-ligands. The CO_2 reacts with the SrO layer to eventually form $SrCO_3$. This type of excessive oxygen supply was diminished when the Ru surface was covered sufficiently with either a blocking TiO_2 layer or thicker STO layer itself. Hence, no growth enhancement and no $SrCO_3$ formation were observed.

Composition and Growth Per Cycle of STO Films. This ALD process allows the growth of STO films with a wide compositional variation on a TiO_2-coated Ru substrate with high reproducibility and accuracy by changing the Ti and Sr cycle ratio (Figure 9a). The Ti compositions of the STO films in Figure 9a exclude the contribution from the thin TiO_2 blocking layer. The Ti concentration [Ti/(Ti + Sr)] increased from 32% to 61% as the Ti:Sr cycle ratio changed from 2:1 to 6:1, and stoichiometric STO films could be deposited at a cycle ratio of 3:1. This is because the rate of SrO incorporation in the film was much higher than that of TiO_2.

The steady state GPC of STO was calculated more precisely from the slope of the thickness vs number of cycles plot. Figure 9b shows the changes in the STO film thickness as a function of the subcycle number on a 5-nm-thick TiO_2 coated Ru substrate when the Ti:Sr cycle ratio was 3:1 and 5:1, respectively. Here, the subcycle number denotes the total number of each cycle for TiO_2 and SrO. For example, the total number of cycles was 400 when (3 TiO_2 cycle + 1 SrO cycle) was repeated 100 times. The figure suggests that the film thickness is directly proportional to the number of ALD cycles. The growth rates were 0.107 and 0.075 nm/cycle when the cycle ratio was 3:1 and 5:1, respectively, and the *y*-axis intercept was ~4.8 nm, which corresponds well to the blocking TiO_2 thickness. The larger

dx.doi.org/10.1021/cm2002572 |*Chem. Mater.* 2011, 23, 2227–2236

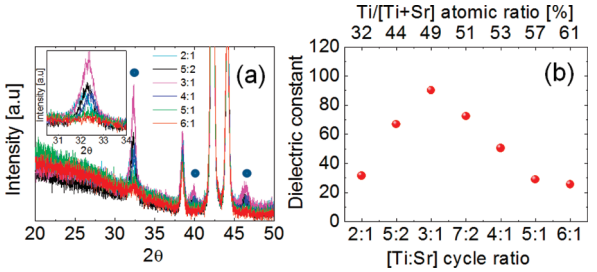

Figure 10. (a) GAXRD patterns of the as-deposited films (18−22 nm) with different Ti:Sr cycle ratios. (Inset) Enlarged (110) peaks from the various samples. (b) Change in the dielectric constants of the thin films (18−22 nm) with the various compositions (also Ti:Sr cycle ratio), where the Ti in the blocking layer was not considered.

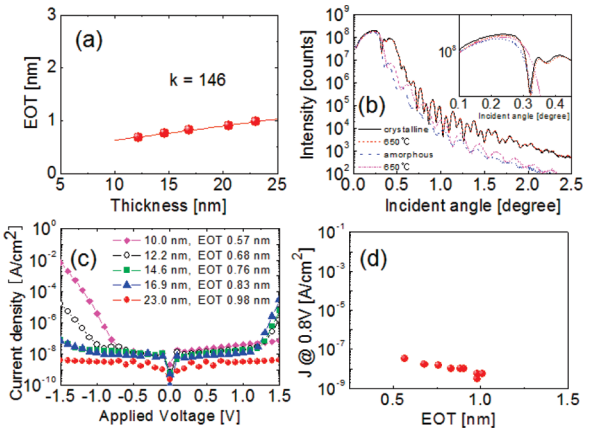

Figure 11. (a) Variation of EOT as a function of physical thickness of STO film where the Ti:Sr cycle ratio was 3:1. The extracted bulk dielectric constant of STO films from the inverse slope of the best linear fitted graph was 146. (b) X-ray reflectivity spectra of the in situ crystallized and amorphous STO films before and after high temperature annealing at 650 °C. (Inset) The enlargement of the critical angle for the clearness. (c) The current density vs applied voltage (J − V) plot of the in situ crystallized STO films with different thicknesses. (d) Summary of the dielectric performance of the STO films. The minimum EOT of 0.57 nm value maintaining a low enough leakage current density (<3 × 10^{-8} Acm^{-2} at ±0.8 V) was achievable from the 10-nm-thick STO film.

growth rate for the 3:1 cycle ratio was attributed to the higher growth rate of the SrO layer than that of the TiO_2 layer. These growth rates were 7 and 5 times faster than that of the ALD STO process using the $Sr(tmhd)_2$ and $Ti(O\text{-}^iPr)_2(tmhd)_2$, respectively.[21] This is a very promising result for mass-production compatibility.

In situ Crystallization and Electrical Properties of STO Films. STO films were grown at different Ti:Sr cycle ratios to examine the dielectric constant as a function of the film composition. The STO films were grown on 3.5-nm-thick TiO_2-coated Ru substrates. After blocking TiO_2 layer deposition, a thin STO seed layer (∼ 4 nm) was deposited under conditions identical to those used for depositing the STO main layer, and the seed layer was annealed at 650 °C for 1 min, which is the optimum condition for crystallization of the seed layer.[21,35] The main STO layer was then grown on the crystalline STO seed layer, which resulted in in situ crystallization of the STO film. Figure 10a shows the GAXRD patterns of the as-deposited films (18−22 nm) with different Ti:Sr cycle ratios. The diffraction peaks confirmed that the presence in situ crystallized STO films with a perovskite structure ((110) at 32.3° and (200) at 46.4 ° and (111) at 39.9 °). The most intensive diffraction peak was observed from the film grown with a cycle ratio of 3:1, which has a maximum dielectric constant and stoichiometric cation composition (Figure 10)). The inset figure shows the enlarged (110) peaks from various samples. The peak positions shifted to lower and higher diffraction angles compared to the stoichiometric film (3:1) with increasing Sr and Ti composition, respectively. This corresponds to the expansion and contraction of the lattice parameters of the crystallized STO film. There is little indication for the formation of a Ruddlesden−Popper phase for the Sr-rich films or TiO_2 for the Ti-rich films. Either these phases have an amorphous structure (or nanocrystalline) that is not detected by XRD or the STO thin film has a wide range of compositions that is not expected from the bulk material. This corresponds to a recent report by another group.[36]

Figure 10b shows the dielectric constants of the thin films (18−22 nm) with various compositions (also Ti:Sr cycle ratios), where the Ti in the blocking layer was not considered. The dielectric constants are rather low (<100) due to the contribution of the interface effect because the dielectric constant was extracted from the measured capacitance and STO film thickness of a one-thickness sample under each condition. The maximum dielectric constant (90) of STO was achieved at a cycle ratio of 3:1, which decreased drastically with increasing or decreasing cycle ratio. To understand the bulk dielectric constant of STO free of the influence of the interfacial layers, the EOT of the STO films with different thickness at a cycle ratio of 3:1 was estimated from the measured capacitance density of each film, and plotted as a function of the physical thickness (t_{phy}). As EOT = t_{phy} ($3.9/\varepsilon_r$), where the ε_r is the bulk dielectric constant of STO, the ε_r, which was extracted from the inverse slope of the best linear fitted graph in Figure 11a, was 146. This is similar to that reported by other authors from a similar ALD process but after PDA at high temperature (550−600 °C).[37] Such a high ε_r value suggests the high quality of the STO film in the present work, even without PDA at high temperatures.

The film density was estimated using a XRR technique (Figure 11b). For this, in situ crystallized and amorphous STO films were prepared by depositing the STO layer on a crystalline STO seed layer on a TiO_2-coated Ru substrate, and directly depositing the STO main layer on Si, respectively. The in situ crystallized STO shows a slightly higher critical angle, where the reflectivity decreases suddenly when the total reflection arises, than that of an amorphous film as shown in the inset figure in Figure 11b. This suggests the higher density of the in situ crystallized film. The XRR spectra were almost identical before and after PDA at 650 °C for the in situ crystallized film. This suggests that the film thickness was not reduced after high temperature annealing owing to its high density. However, in the case of amorphous STO, the spectrum was changed after the same PDA. In particular, the critical angle was increased to a higher value, which indicates the increase in density after annealing. The XRR results show that the in situ crystallization of the STO film was crucial for achieving structural robustness.

Figure 11c shows the current density vs applied voltage (J − V) plots of the in situ crystallized STO films with different thicknesses. The 12.2-nm-thick film showed an EOT of 0.68 nm and a very low leakage current density (∼ 2 × 10^{-8} Acm^{-2}) within the −1 V to +1 V region. Figure 11d summarizes the dielectric performance of the STO films. The minimum EOT

dx.doi.org/10.1021/cm2002572 |Chem. Mater. 2011, 23, 2227–2236

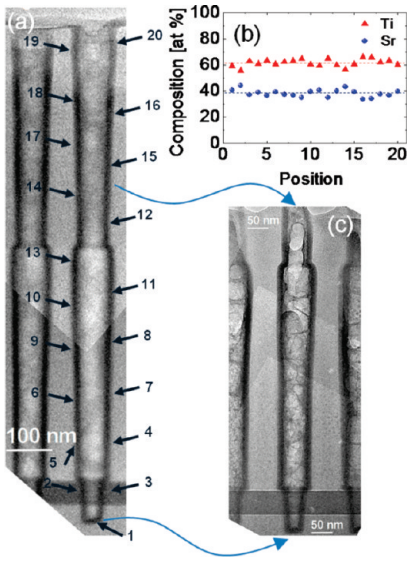

Figure 12. (a)−(c) Cross-section transmission electron microscopy and energy dispersive spectroscopy results that show a highly conformal thickness as well as composition step coverage (>95%) of the STO film inside a capacitor hole structure deposited at 370 °C. The opening diameter is 108 nm and the hole depth is 1.08 μm, giving an aspect ratio of ∼10.

value of 0.57 nm maintaining a low enough leakage current density (∼ 3×10^{-8} Acm^{-2} at ±0.8 V) was achieved from a stoichiometric STO film as thin as 10 nm. This is very promising for the DRAM capacitors with the design rule of <30 nm. An interesting finding from the further reduction of the physical thickness of the STO film was that the EOT value was actually increased (data not shown). This suggests that the crystallization behavior of the very thin (≪ 10 nm) STO films are quite dependent on the film thickness. Details of this thickness-dependent in situ crystallization behavior will be reported elsewhere.

Step Coverage of STO Film. The cross-section TEM and EDS results in Figure 12a−c, respectively, show the highly conformal thickness as well as the composition step coverage (>95%) of the STO film inside a capacitor hole structure deposited at 370 °C. The opening diameter and hole depth were 108 nm and 1.08 μm, respectively, giving the hole an aspect ratio of ∼10. These results suggest that the self-limited ALD reaction occurred uniformly all over the capacitor hole area.

IV. CONCLUSIONS

STO thin films were grown on Ru-coated Si wafers by ALD using $Ti(O\text{-}^iPr)_2(tmhd)_2$ and $Sr(^iPr_3Cp)_2$ as metal organic precursors at a typical T_g of 370 °C. O_3 and H_2O were used as the oxygen sources for TiO_2 and SrO layer growth, respectively. In contrast to a previous report on the ALD of STO using the $Sr(tmhd)_2$, the same Ti-precursor and H_2O, where a GPC of only 0.015 nm/cycle was achieved,[21] this process resulted in a highly improved GPC. The steady state GPC of a stoichiometric STO film was 0.107 nm/subcycle (0.428 nm/supercycle), which is ∼7 times higher than previously reported. Even with such a high growth rate, very promising dielectric performance as well as a high degree of structural and compositional conformality over severe three-dimensional capacitor structures was achieved. A minimum EOT of 0.57 nm with a low enough leakage current was achieved. A bulk dielectric constant of 146 was achieved from stoichiometric STO films without PDA at high temperature. The in situ crystallization of the STO film was the key factor for acquiring such promising dielectric films. The enhanced initial growth of the TiO_2 and SrO layers on a Ru substrate surface, which is detrimental to reproducible film growth, was understood from the effect of oxygen supplied from the substrate during the precursor pulse steps. This was suppressed by adopting a thin (<5 nm) TiO_2 blocking layer prior to STO growth. This process and STO thin film material are very promising for use in mass-production compatible DRAM capacitor fabrication processes with the design rule of <30 nm. The present blocking layer thickness (3.5∼5 nm) is slightly excessive considering the extremely limited space allowed for the dielectric films in highly scaled DRAMs. Furthermore, the in situ crystallization appears to be thickness dependent when the film thickness becomes very thin (≪ 10 nm). Therefore, further research on the ultimate thickness scaling on both the blocking layer and STO high dielectric films is necessary.

AUTHOR INFORMATION

Corresponding Author

*E-mail: cheolsh@snu.ac.kr.

ACKNOWLEDGMENT

This study was supported by the IT R&D program of MKE/KEIT [KI002178, Development of a mass production compatible capacitor for next generation DRAM], Converging Research Center Program through the National Research Foundation of Korea (NRF) funded by the Ministry of Education, Science and Technology (2010K000977), and WCU (World Class University) program through National Research Foundation of Korea funded by the Ministry of Education, Science and Technology (R31-2008-000-10075-0).

REFERENCES

(1) Kim, S. K.; Lee, S. W.; Han, J. H.; Lee, B.; Han, S.; Hwang, C. S. *Adv. Funct. Mater.* **2010**, *20*, 2989.
(2) Cho, H. J.; Kim, Y. D.; Park, D. S.; Lee, E.; Park, C. H.; Jang, J. S.; Lee, K. B.; Kim, H. W.; Ki, Y. J.; Han, I. K.; Song, Y. W. *Solid-State Electron.* **2007**, *51*, 1529.
(3) Kim, S. K.; Choi, G.-J.; Lee, S. Y.; Seo, M.; Lee, S. W.; Han, J. H.; Ahn, H.-S.; Han, S.; Hwang, C. S. *Adv. Mater.* **2008**, *20*, 1429.
(4) Hwang, C. S.; Park, S. O.; Kang, C. S.; Cho, H. J.; Kang, H. K.; Ahn, S. T.; Lee, M. Y. *Jpn. J. Appl. Phys.* **1995**, *34*, 5178.
(5) Park, S. O.; Hwang, C. S.; Kang, C. S.; Cho, H. J.; Lee, S. I.; Lee, M. Y. *Jpn. J. Appl. Phys.* **1996**, *35*, 1548.
(6) Kuroiwa, T.; Tsunemine, Y.; Horikawa, T.; Makita, T.; Tanimura, J.; Mikami, N.; Sato, K. *Jpn. J. Appl. Phys.* **1994**, *33*, 5187.
(7) Takemura, K.; Sakuma, T.; Miyasaka, Y. *Appl. Phys. Lett.* **1994**, *64*, 2967.
(8) Hwang, C. S.; Kang, C. S.; Cho, H. J.; Park, S. O.; Lee, B. T.; Kim, J. W.; Horii, H.; Lee, S. I.; Lee, M. Y. *Integr. Ferroelectr.* **1996**, *12*, 199.
(9) Kang, C. S.; Hwang, C. S.; Cho, H. J.; Lee, B. T.; Park, S. O.; Kim, J. W.; Horii, H.; Lee, S. I.; Lee, M. Y. *Jpn. J. Appl. Phys.* **1996**, *35*, 4890.
(10) Kawahara, T.; Yamamuka, M.; Yuuki, A.; Ono, K. *Jpn. J. Appl. Phys.* **1995**, *34*, 5077.
(11) Yamaguchi, H.; Lesaicherre, P. Y.; Sakuma, T.; Miyasaka, Y.; Ishitani, A.; Yoshid, M. *Jpn. J. Appl. Phys.* **1993**, *32*, 4069.
(12) Hwang, C. S.; Park, J.; Hwang, D. S.; Yoo, C. Y. *J. Electrochem. Soc.* **2001**, *148*, G636.
(13) Hwang, C. S.; No, S. Y.; Park, J.; Kim, H. J.; Cho, H. J.; Han, Y. K.; Oh, K. Y. *J. Electrochem. Soc.* **2002**, *149*, G585.

(14) Kil, D. S.; Lee, J. M.; Roh, J. S. *Chem. Vap. Deposition* **2002** *8* (5), 195.
(15) Lee, J. H.; Cho, Y. J.; Min, Y. S.; Kim, D.; Rhee, S. W. *J. Vac. Sci. Technol. A* **2002**, *20* (5), 1828.
(16) Menou, N.; Popovici, M.; Clima, S.; Opsomer, K.; Polspoel, W.; Kaczer, B.; Rampelberg, G.; Tomida, K.; Pawlak, M. A.; Detavernier, C.; Pierreux, D.; Swerts, J.; Maes, J. W.; Manger, D.; Badylevich, M.; Afanasiev, V.; Conard, T.; Favia, P.; Bender, H.; Brijs, B.; Vandervorst, W.; Van Elshocht, S.; Pourtois, G.; Wouters, D. J.; Biesemans, S.; Kittl, J. A. *J. App. Phys.* **2009**, *106*, 094101. Also Pawlak, M. A.; Kaczer, B.; Kim, M. -S.; Popovici, M.; Tomida, K.; Swerts, J.; Opsomer, K.; Polspoel, W.; Favia, P.; Vrancken, C.; Demeurisse, C.; Wang, W. −C.; Afanasiev, V.; Vandervorst, W.; Bender, H.; Debusschere, I.; Altimime, L.; Kittl, J. A. *App. Phys. Lett.* **2010**, *97*, 162906.
(17) Vehkamäki, M.; Hatanpää, T.; Hänninen, T.; Ritala, M.; Leskelä, M. *Electrochem. Solid-State Lett.* **1999**, *2*, 504.
(18) Vehkamäki, M.; Hänninen, T.; Ritala, M.; Leskelä, M.; Sajavaara, T.; Rauhala, E.; Keinonen, J. *Chem. Vap. Deposition* **2001**, *7*, 75.
(19) Kosola, A.; Putkonen, M.; Johansson, L.-S.; Niinistö, L. *Appl. Surf. Sci.* **2003**, *211*, 102.
(20) Ahn, J. H.; Kim, J. Y.; Kang, S. W.; Kim, J. H.; Roh, J. S. *Appl. Phys. Lett.* **2007**, *91*, 062910.
(21) Lee, S. W.; Kwon, O. S.; Han, J. H.; Hwang, C. S. *Appl. Phys. Lett.* **2008**, *92*, 222903.
(22) Kwon, O. S.; Lee, S. W.; Han, J. H.; Hwang, C. S. *J. Electrochem. Soc.* **2007**, *154*, G127.
(23) Holme, T. P.; Prinz, F. B. *J. Phys. Chem. A* **2007**, *111*, 8147.
(24) Lee, S. W.; Han, J. H.; Kim, S. K.; Han, S.; Lee, W.; Hwang, C. S. *Chem. Mater.* **2011**, *23*, 976.
(25) Aarik, J.; Aidla, A.; Uustare, T.; Ritala, M.; Leskela, M. *Appl. Surf. Sci.* **2000**, *161*, 385.
(26) Lee, H. J.; Park, M. H.; Min, Y-S; Clavel, G.; Pinna, N.; Hwang, C. S. *J. Phys. Chem. C* **2010**, *114*, 12736.
(27) Goldstein, D. N.; McCormick, J. A.; George, S. M. *J. Phys. Chem. C* **2008**, *112*, 19530.
(28) Rai, V. R.; Agarwal, S. *J. Phys. Chem. C* **2008**, *112*, 9552.
(29) Iwahori, K.; Watanabe, S.; Kawai, M.; Mizuno, K.; Sasaki, K.; Yoshimoto, M. *J. Appl. Phys.* **2000**, *88*, 7099.
(30) Guhl, H.; Miller, W.; Reuter, K. *Phys. Rev. B* **2010**, *81*, 155455.
(31) NIST. X-ray Photoelectron Spectroscopy Database. http://srdata.nist.gov/xps/.
(32) Moulder, J. F.; Stickle, W. F.; Sobol, P. E.; Bomben, K. D. In *Handbook of X-Ray Photoelectron Spectroscopy*; Chastain, J., Ed.; Perkin-Elmer: Eden Prairie, MN, 1992; p 179.
(33) Barin, I. *Thermochemical Data of Pure Substances*; VCH: Weinheim, 1989; Part II, pp 1254 and 1433.
(34) Won, S. J.; Suh, S.; Lee, S. W.; Choi, G. J.; Hwang, C. S.; Kim, H. J. *Electrochem. Solid-State Lett.* **2010**, *13* (2), G13.
(35) Lee, S. W.; Han, J. H.; Kwon, O. S.; Hwang, C. S. *J. Electrochem. Soc.* **2008**, *155* (11), G253.
(36) Popovici, M.; Van Elshocht, S.; Menou, N.; Swerts, J.; Pierreux, D.; Delabie, A.; Brijs, B.; Conard, T.; Opsomer, K.; Maes, J. W.; Wouters, D. J.; Kittl, J. A. *J. Electrochem. Soc.* **2010**, *157*, G1.
(37) Clima, S.; Pourtois, G.; Menou, N.; Popovici, M.; Rothschild, A.; Kaczer, B.; Van Elshocht, S.; Wang, X. P.; Swerts, J.; Pierreux, D.; De Gendt, S.; Wouters, D. J.; Kittl, J. A. *Microelectron. Eng.* **2009**, *86*, 1936.